Plasma properties as function of time in Ar/C2H2 dust-forming plasma

Igor Denysenko, Eric von Wahl, Maxime Mikikian, Johannes Berndt, Sergii Ivko, Holger Kersten, Eva Kovacevic, Nikolay A. Azarenkov

Plasma properties as function of time in Ar/C_2H_2 dust-forming plasma

I B Denysenko[1,2,3], E von Wahl[2,4], M Mikikian[2], J Berndt[2], S Ivko[1], H Kersten[4],

E Kovacevic[2] and N A Azarenkov[1]

[1] School of Physics and Technology, V N Karazin Kharkiv National University, Kharkiv, Ukraine
[2] GREMI, UMR7344 CNRS/Université d'Orléans, F-45067 Orléans, Cedex 2, France
[3]Le Studium, Loire Valley Institute for Advanced Studies, Orléans & Tours, France
[4]Institut für Experimentelle und Angewandte Physik, Christian-Albrechts-Universität zu Kiel, Kiel, Germany

E-mail: idenysenko@yahoo.com

Received
Accepted for publication
Published

Abstract

The time-dependent properties of an Ar/C_2H_2 dusty plasma (neutral, ion and electron densities, effective electron temperature and dust charge) are studied using a volume-averaged model for conditions corresponding to experiments on nanoparticle growth. The calculated density evolution for C_2H_2, H_2 and C_4H_2 molecules are compared with time-resolved measurement of the mass peaks of the neutral species and the effects of the dust density on the plasma properties are analyzed. Time evolutions of the main positive and negative ions are also obtained thanks to the calculations. As a consistency check the time-dependence of the dust radius is also obtained numerically, assuming that an increase of the dust radius is due to deposition of hydrocarbon ions and C_2H radicals on the surface of dust particles. It is shown that for conditions corresponding to the experiment, the ions are the main contributor to the particle growth. The calculated dust growth rate is compared to the time-dependence of the dust particle size obtained in the experimental measurements. The results of the numerical calculations are found to be in a good qualitative agreement with the experimental data.

Keywords: argon/acetylene plasma, nanoparticles, time-dependence, volume-averaged model

1. Introduction

Reactive plasmas containing growing nano-and micrometer-sized particles (dust particles) are of a great fundamental interest due to various useful technological applications [1–4]. For the growth of carbonaceous dust particles, gas discharges from methane, acetylene or ethylene are usually used [5–7]. To control the dust particle growth, these discharges have been intensively investigated by many authors [5–22].

Experiments in Ar/C_2H_2 plasmas revealed that formation of dust particles is accompanied by a decrease of electron and acetylene densities and by an increase of electron temperature and density of metastable argon atoms [10–13]. In [13, 23], it was also shown that the degree of dissociation of acetylene can be as high as 99%. In [24], nanoparticles from a dusty Ar/C_2H_2 plasma were extracted and the average dust particle diameter as a function of time was determined. Numerous experiments also revealed that the formation of nanoparticles in Ar/C_2H_2 plasmas exhibits a periodical behavior [11, 15, 25]. It is widely accepted that the formation is characterized by a few stages [1, 25]. In a first stage which is mainly driven by plasma chemical reactions, stable, nanometer sized protoparticles or clusters are produced [25]. After this *nucleation* stage, the *coagulation* stage takes place when the protoparticles frequently collide with each other resulting in the formation of dust particles with sizes up to several tens of nanometers. The third and slowest growth stage is the *accretion* stage where radicals and ions from plasma stick to the dust particles. However, it is unclear at present which

species (ions or radicals) affect more essentially the nanoparticle growth in the accretion stage. In [26], it was found experimentally that the diameter of dust particles increases during the accretion stage nearly linearly in time. It was also concluded that the particles grow nearly monodisperse, i.e., their size distribution is very narrow [24, 26]. At the end of the accretion stage the dust particles reach a maximum size (a few hundred nanometers) and leave the discharge because of the interplay of different forces on the dust particles, and then a new growth cycle starts.

C_2H_2 and Ar/C_2H_2 RF plasmas have already been studied by computer simulations [16–21, 27]. The studies allowed to explain the nucleation of nanoparticles in these chemistries. It was shown that both positive and negative ions may participate as precursors in the initial stage of particle formation [17, 19]. Meantime, most of these numerical studies considered only the nucleation stage of particle formation and, therefore, they did not account for effects of dust particles on plasma properties, which are usually important as seen in experiments. Effects of dust particles on Ar/C_2H_2 plasmas in glow and afterglow regimes were studied in [15, 28], using a volume averaged model, and the results for the glow plasma were compared with mass spectrometry measurements. It was found that due to collection of electrons and ions by dust particles, the effective electron temperature, the densities of argon ions and metastable argon atoms are larger in the dusty glow plasma comparing with the dust-free case, while the densities of most hydrocarbon ions and acetylene molecules are smaller [15]. Note that most of numerical studies on Ar/C_2H_2 and C_2H_2 plasmas were carried out using steady-state models that do not fully consider the dusty plasma dynamics with periodical growth of nanoparticles and variation of dust radius with time.

In this paper, we present the time-dependencies of plasma properties (ion, electron and neutral particle densities, effective electron temperature and dust charge) in an Ar/C_2H_2 dusty plasma obtained using a global (volume-averaged) model. Effects of growing dust particles in the plasma volume on the plasma properties are investigated. The calculated evolution of the densities of C_2H_2, H_2 and C_4H_2 molecules are compared to the measured time-dependencies for the mass peaks of the neutral species. We also obtain the dust radius as a function of time for the accretion stage. The calculations are carried out assuming that the growth is due to deposition of hydrocarbon ions and C_2H radicals on the dust particles. The calculation results for the dust growth rate are compared to those obtained from experimental measurements.

2. Theoretical model

2.1. Main assumptions and equations

In the model, it is assumed that the Ar/C_2H_2 gas-discharge plasma has R = 22 cm radius and L = 32.4 cm height and is sustained in a cylindrical stainless-steel chamber. The input fluxes of acetylene and argon are Q_{C2H2} (=1.5 sccm) and argon Q_{Ar} (=11.0 sccm), respectively. The plasma is driven at a RF power of 9 W by a RF generator. The external parameters are taken to be nearly the same as in the experiment [15, 24]. The plasma consists of electrons with density n_e, seven positive ions with densities n_α^+ (where the index α = C2H2, Ar, ArH, C4H3, C4H2, C6H4 and C2H3 corresponds to the $C_2H_2^+$, Ar^+, ArH^+, $C_4H_3^+$, $C_4H_2^+$, $C_6H_4^+$ and $C_2H_3^+$ ions, respectively), six neutrals (four nonradical and two radical) with densities n_α (where the index α = Ar, C2H2, H2, C4H2 corresponds to the nonradical neutrals Ar, C_2H_2, H_2, C_4H_2, respectively, and α = C2H, H is for the radicals C_2H and H, correspondingly), negatively charged dust particles with density n_d, radius a_d and charge Z_d (in units of electron charge), metastable argon atoms (Ar_m) with density n_m, argon atoms in the resonance 4s states ($^3P_1$ and $^1P_1$) (Ar_r) with density n_r as well as argon atoms in 4p states (Ar(4p)) with density n_{4p}. In our model, the metastable and resonance atom densities n_m, n_r and n_{4p} represent the density of a composite ($^3P_0$ and $^3P_2$) metastable level, the density of a composite ($^3P_1$ and $^1P_1$) resonance level and the density of a composite 4p state, respectively. The model accounts for main positive ions and neutral species identified in our experimental measurements on mass spectra of positive ions and neutral species [15, 28]. We do not account for H^+ and H_2^+ ions here because our previous experimental and numerical studies [15, 28] showed that the densities of these ions in the Ar/C_2H_2 gas-discharge are small while the collision rates of H^+ and H_2^+ with other plasma species are in the same order of magnitude as the corresponding rates for collisions of other positive ions.

We also assume that the plasma contains negative ions C_2H^-, C_4H^- and C_6H^- with densities n_{C2H-}, n_{C4H-} and n_{C6H-}, respectively. At large ratio n_{Ar}/n_{C2H2}, the anions C_2H^- are the dominant negative ions [20, 21]. On the contrary, in pure C_2H_2 plasmas, larger anions, like $C_{12}H^-$ and C_6H^- are dominant [6, 17, 18]. The dominant neutral species are argon atoms with density $n_{Ar} \approx P/(k_B T_g)$, where P = 4.2 Pa is the pressure of argon gas and k_B is the Boltzmann constant.

We assume that the energy distribution for ions is Maxwellian, and that the ions and dust particles are at gas temperature T_g (300 K).

It is assumed that the electron energy distribution function (EEDF) F has a Druyvesteyn shape [29]:

$$F(\varepsilon) = A_1 \varepsilon^{1/2} \exp(-A_2 \varepsilon^2), \quad (1)$$

where ε is the electron energy and A_1 and A_2 are functions of the average electron energy [29] $\langle \varepsilon \rangle = \int_0^\infty \varepsilon F(\varepsilon) d\varepsilon = \frac{3}{2} e T_{\text{eff}}$ and T_{eff} is the effective electron temperature. The EEDF has the following normalization $\int_0^\infty F(\varepsilon) d\varepsilon = 1$.

The Druyvesteyn distribution is typical for RF plasmas under conditions considered here [30].

The plasma is assumed to be quasineutral, or

$$\sum_{\alpha} n_{\alpha}^{+} = n_e + n_{C2H-} + n_{C4H-} + n_{C6H-} + |Z_d| n_d . \qquad (2)$$

The density of a species X (ions or neutrals) is obtained from the balance equation

$$\frac{dn^{(X)}}{dt} = \sum_i R_{G,i}^{(X)} - \sum_i R_{L,i}^{(X)} , \qquad (3)$$

where $R_{G,i}^{(X)}$ and $R_{L,i}^{(X)}$ are, respectively, the rates for reactions describing various generation and loss processes of the species X and t is the time. Here, we consider various processes for the loss and generation of the discharge species, including the processes on plasma walls and dust particles, the collisional processes in the bulk plasma, as well as the pumping of gas in and out of the chamber. The processes are detailed in the next subsection.

The effective electron temperature is found from the power balance equation

$$\frac{d}{dt}\left(\frac{3}{2} e n_e T_{\text{eff}}\right) = \frac{1}{V}(P_{abs} - P_{loss}), \qquad (4)$$

where P_{abs} = 9 W is the absorbed power, V is the volume of the discharge chamber, the power loss $P_{loss} = P_{coll} + P_w + P_d$, where P_{coll} is the power loss due to elastic and inelastic electron-neutral collisions, P_w and P_d are the power losses due to charged particle fluxes to the walls and to the dust particles, respectively. Here $P_{coll} = e n_e V \sum_{\alpha} n^{(\alpha)} \varepsilon_c^{(\alpha)} k_{iz}^{(\alpha)}$, V is the volume of the discharge chamber, $\varepsilon_c^{(\alpha)} = \varepsilon_{iz}^{(\alpha)} + \sum_i \varepsilon_{ex,i}^{(\alpha)} \frac{k_{ex,i}^{(\alpha)}}{k_{iz}^{(\alpha)}} + \frac{k_{el}^{(\alpha)}}{k_{iz}^{(\alpha)}} \frac{3m_e}{m^{(\alpha)}} T_{\text{eff}}$ [31, 32], $\boldsymbol{\varepsilon}_{iz}^{(\alpha)}$ is the ionization energy of neutrals α and $\boldsymbol{\varepsilon}_{ex,i}^{(\alpha)}$ is the energy for the i-th excitation or dissociation process of neutrals α. $k_{ex,i}^{(\alpha)}$ and $k_{iz}^{(\alpha)}$ are, respectively, the rate coefficients for the ith excitation or dissociation process and the ionization rate coefficient of species α. $k_{el}^{(\alpha)}$ is the elastic scattering rate coefficient of neutrals $\boldsymbol{\alpha}$, $n^{(\alpha)}$ and $\boldsymbol{m}^{(\alpha)}$ are, respectively, the density and mass of neutral species. $P_w = \sum_j e n_j^{+} u_{Bj} 2\pi A_{effj} (\varepsilon_i + \varepsilon_e)$, $\varepsilon_i = \frac{[\Gamma(\xi_1)]^2}{\Gamma(\xi_2)\Gamma(\xi_3)} \langle \varepsilon \rangle + V_s$ is the mean kinetic energy lost per ion [31] and $\varepsilon_e = \frac{\Gamma(\xi_1)\Gamma(\xi_5)}{\Gamma(\xi_2)\Gamma(\xi_4)} \langle \varepsilon \rangle$ is the mean kinetic energy lost per electron [31], where $\Gamma(\xi)$ is the gamma function with $\xi_1 = 3/2x$, $\xi_2 = 5/2x$ $\xi_3 = 1/2x$, $\xi_4 = 2/x$, $\xi_5 = 3/x$ and $x = 2$. $V_s \approx -T_{\text{eff}} x^{-0.43} \ln(4.0 u_{BAr+} / \bar{\upsilon}_e)$, $\bar{\upsilon}_e = \langle \varepsilon \rangle^{1/2} \left(\frac{2e}{m_e}\right)^{1/2} \frac{\Gamma(\xi_4)}{[\Gamma(\xi_1)\Gamma(\xi_2)]^{1/2}}$ is the mean electron speed and $u_{Bj} = \langle \varepsilon \rangle^{1/2} \left(\frac{2e}{m_j}\right)^{1/2} \frac{\Gamma(\xi_1)}{[\Gamma(\xi_2)\Gamma(\xi_3)]^{1/2}}$ is the Bohm velocity [31]. The expression for A_{effj} will be presented in the next subsection. The term describing the energy loss on dust particles is [33] $P_d \approx e\pi a_d^2 n_d n_e V \int_{-e\Phi_s}^{\infty} \varepsilon(1 + e\Phi_s/\varepsilon)\sqrt{2e\varepsilon/m_e} F(\varepsilon) d\varepsilon$, where $\Phi_s = eZ_d / a_d$ is the dust surface potential.

The dust charge Z_d is found from the following equation

$$\frac{\partial |Z_d|}{\partial t} = K_d^e n_e - \sum_{\alpha} K_d^{\alpha} n_{\alpha}^{+}, \qquad (5)$$

where the rates K_d^e and K_d^{α} describe, respectively, collection of electrons and positive ions of sort α by the dust particles. $K_d^e = \pi a_d^2 \int_{-\Phi_s}^{\infty} (1 + e\Phi_s/\varepsilon)\sqrt{2e\varepsilon/m_e} F(\varepsilon) d\varepsilon$ and $K_d^{\alpha} \approx a_d^2 \left(8\pi e T_i / m_{\alpha}^{+}\right)^{1/2} \left(1 + \xi\tau + H\xi^2\tau^2 \lambda_s n_a \sigma_{ia}\right)$. Here $\tau = T_{\text{eff}} / T_i$, $\xi = |Z_d| e^2 / a_d T_{\text{eff}}$, T_i is the ion temperature, m_e and m_{α} are, respectively, the masses of electrons and positive ions of sort α. σ_{ia} ($\approx 10^{-14}$ cm^2) is the cross-section for ion-atom collisions. The function H satisfies $H \sim 0.1$ for $0.1 \le \beta \le 10$, $H \sim \beta$ for $\beta << 1$ and $H \sim \beta^{-2} (\ln\beta)^3$ for $\beta >> 1$ [34], where $\beta = |Z_d| e^2 / \lambda_s T_i$, and λ_s is the screening length, which is of the same order as the Debye length [1].

The balance equations for neutrals and ions, the power balance equation and the equation for dust charge are solved by using the DVODE package [35]. Solving these equations, we assume that the dust density and dust radius are known at each instant. First, the system of first order differential equations is allowed to reach a steady state, i.e. d/dt = 0, for the case when the dust particles are absent from the plasma. After reaching the steady state, it is assumed that the dust radius increases linearly from 10 nm up to 70 nm at a fixed dust density (~ 10^7 cm^{-3}) during 88 s. This is supported by our experimental measurements that show this size evolution with a quite narrow size distribution throughout the entire accretion phase with 10 nm sized particles being the smallest ones having been collected. At the end of the phase (when a_d = 70 nm), we suppose that the dust particles leave the plasma (because of effect of different forces on the dust grains). After the particle leaving, it is assumed that the dust particles do not affect much the plasma (n_d = 0) during next 20 s. After that, a new growth cycle starts.

Making use of the calculated densities of plasma species, effective electron temperature and dust charge (equations (1)-(5)) at the assumption that dust radius grows linearly with time in the accretion stage, one can find the approximate time-

dependence for the dust radius a_d^{approx} from the following expression:

$$\frac{da_d^{approx}}{dt} = \frac{\sum_\alpha K_d^\alpha m_\alpha^+ n_\alpha^+ + K_d^{C2H} m_{C2H} n_{C2H}}{4\pi\rho_d (a_d^{approx})^2}, \qquad (6)$$

where m_{C2H} is the mass of C_2H molecule, $K_d^{C2H} = \gamma_{st}\pi a_d^2(t)\left(8k_BT_g/\pi m_{C2H}\right)^{0.5}$, γ_{st} = 0.9 is the sticking coefficient for collisions of C_2H radicals with dust particles, which is taken to be the same as that for collisions of the radicals with the walls [17, 36]. ρ_d is the dust material density and the index α is related to hydrocarbon positive ions. The calculations are carried out for ρ_d = 1.0, 1.5 and 2.0 g/cm^3 (typical values for the wide variety of carbon based materials [37, 38]).

Note that equation (6) is not used to calculate the time-dependence for dust radius self-consistently with other plasma parameters. It is used to estimate impacts of ions and radicals on the growth of nanoparticles.

2.2. The rates for various generation and loss processes

The rate due to the flow of acetylene into a chamber of volume *V* is given by $R = J_{C2H2} = 4.48\times10^{17} Q_{C2H2}/V$ [31, 39], where Q_{C2H2} (=1.5 sccm) and the scalar converts sccm to cm^{-3}s^{-1}. The rate at which particles *X* leave the discharge due to pumping is $R = \upsilon_{pump} n^{(X)}/V$, where υ_{pump} is the pumping rate in cm^3/s. Taking into account that the flow rate of argon is approximately equal to the argon pumping rate (since the plasma is low-ionized), one can estimate the pumping rate $\upsilon_{pump} \approx J_{Ar} V / n_{Ar}$, where $J_{Ar} = 4.48\times10^{17} Q_{Ar}/V$ and Q_{Ar}=11.0 sccm.

The rate describing the radical loss due to diffusion to the walls is $R_w^r = K_w^r n_r$ (here the index *r* corresponds to the hydrogen atoms or C_2H molecules), where $K_{wall}^r = \left[\Lambda_n^2/D_n + 2V(2-\gamma_r)/(S_{surf}\upsilon_{thr}\gamma_r)\right]^{-1}$ [31, 40]. γ_r is the sticking coefficient for the neutral particle on the wall surface, $\upsilon_{thr} = \sqrt{8k_BT_g/\pi m_r}$ is the mean velocity of species *r*, m_r is the mass of species *r*, S_{surf} is the wall surface area of the reactor chamber, D_n is the neutral diffusion coefficient, $\Lambda_n = \left[(\pi/L)^2 + (2.405/R)^2\right]^{-1/2}$ is the effective diffusion length. The neutral diffusion coefficients were calculated in the same manner as in [17, 20]. The binary collision diameters, potential energies and polarizabilities of the background gases, which are necessary for the calculation of the diffusion coefficients of neutrals and ions, were taken from [17, 19, 41]. The sticking coefficient is a function of the radical species, the surface material, the surface condition (for example, substrate temperature and roughness) and even the plasma parameters (for example, ion flux) [42, 43]. Formation of thin films on the chamber walls during the growth of nanoparticles in the plasma volume can also affect the sticking coefficients [44]. The sticking coefficients for C_2H and H radical neutrals are assumed to be 0.9 and 0.1, respectively [17, 42, 45].

For the radical neutrals and metastable argon atoms, it is accounted for their deposition on dust particles, and the rate describing the loss process in equation (3) is taken to be $R = K_d^r n_r n_d$, where $K_d^r = \pi a_d^2\left(8k_BT_g/\pi m_r\right)^{0.5}$. The rates describing the positive ion and electron losses on dust particles are $K_d^e n_e n_d$ and $K_d^\alpha n_\alpha^+ n_d$, respectively. We do not account for negative ion deposition on dust particles because their energy is essentially smaller than the dust surface potential.

To determine the rates describing the ion losses on the plasma walls, we obtained the ion mobility μ_j and the ion diffusion coefficient D_j for a *j*-th ion. The mobility of the *j*-th ions in the mixture of gases can be calculated in the same way as the diffusion coefficient of a neutral particle, by Blanc's law, $P_{tot}/\mu_j = \sum_i (P_i/\mu_{ij})$, where P_{tot} is the total gas pressure in pascals and P_i is the partial gas pressure. The ion mobility of the ionic species *j* in the background gas *i* (in m^{2}V^{-1}s^{-1}) can be calculated from the following expression [46]:

$$\mu_{ij} = 0.514(m_{ij}\alpha_i)^{-0.5} T_g / P_{tot},$$

where α_i (in $\mathring{A}^3$) is the polarizability of the background gas *i* [17, 19, 41] and m_{ij} is the reduced ion mass in amu. Then the diffusion coefficient for the *j*-th ion can be derived from the Einstein relation, $D_j = k_BT_{ion}\mu_j/e$, where $T_{ion} = T_g$ is the ion temperature. Using the expression for D_j, one can get the ambipolar diffusion coefficient for the *j*-th ion, $D_{aj} = D_j(1 + eT_{\text{eff}}/k_BT_{ion})$, and the ion mean-free path [31], $\lambda_j = D_j\upsilon_j m_j / k_BT_{ion}$, where m_j is the mass of *j*-th ion, and $\upsilon_j = \sqrt{8k_BT_{ion}/\pi m_j}$ is its average velocity. Using the expressions, the rate in equation (3) describing the loss of the *j*-th positive ion on the plasma walls is given by $R = K_{wj} n_j^+$ [31], where $K_{wj} = 2u_{Bj}\frac{A_{effj}}{R^2L}$, $A_{effj} = R^2h_{Lj} + RLh_{Rj}$, $h_{Lj} = \sqrt{h_{aLj}^2 + h_{bLj}^2 + h_{cj}^2}$ and $h_{Rj} = \sqrt{h_{aRj}^2 + h_{bRj}^2 + h_{cj}^2}$. Here $h_{aLj} \approx \frac{0.86}{1+\alpha_0}\left[3.0 + \frac{L}{2\lambda_j}\right]^{-1/2}$, $h_{aRj} \approx \frac{0.8}{1+\alpha_0}\left[4.0 + \frac{R}{\lambda_j}\right]^{-1/2}$, $\alpha_0 = \frac{3}{2}\frac{n^-}{n_e}$, $n^- = n_{C2H-} + n_{C4H-} + n_{C6H-}$,

$$h_{bLj} \approx \frac{\alpha_0}{1+\alpha_0}\left[\sqrt{\frac{eT_{\text{eff}}}{k_B T_{ion}}}\left(1+\frac{L}{2\sqrt{2\pi}\lambda_j}\right)\right]^{-1},$$

$$h_{bRj} \approx \frac{\alpha_0}{1+\alpha_0}\left[\sqrt{\frac{eT_{\text{eff}}}{k_B T_{ion}}}\left(1+\frac{R}{\sqrt{2\pi}\lambda_j}\right)\right]^{-1},$$

$$h_{cj} \approx \left[\sqrt{\frac{eT_{\text{eff}}}{k_B T_{ion}}}\left(1+\frac{n_{j*}^{1/2} n_j^+}{(n^-)^{3/2}}\right)\right]^{-1}, \qquad n_{j*} = \frac{15}{56}\sqrt{\frac{8k_B T_{ion}}{\pi m_j}}\frac{1}{K_{recj}\lambda_j}$$

[47 - 49] and K_{recj} is the rate for collisions of negative ions with *j*-th positive ions. K_{recj} = 1.01×10^{-7} cm^3/s, 5.0×10^{-8} cm^3/s, 3.0×10^{-8} cm^3/s, 3.0×10^{-8} cm^3/s and 1.7×10^{-7} cm^3/s for the reactions $C_{2n}H^- + Ar^+ \rightarrow C_{2n}H + Ar$, $C_{2n}H^- + C_mH_n^+ \rightarrow C_{2n}H + C_mH_n$, $C_{2n}H^- + ArH^+ \rightarrow C_{2n}H + H + Ar$, $C_{2n}H^- + H^+ \rightarrow C_{2n}H + H$ and $C_{2n}H^- + H_2^+ \rightarrow C_{2n}H + 2H$, respectively. Here n =1,2,3.

Considering various collisional processes in the plasma volume, we accounted only for binary collisions. A reaction rate for such reactions is calculated as the product of the reactant densities and the rate coefficient K of the reaction, $R = K \times n_\alpha n_\beta$, where n_α and n_β are the densities of the reactants. The reactions for collisions of negative ions with positive ions and neutrals, taken into account in our study, are presented in table 1.

Table 1. Reactions for collisions of negative ions with positive ions and neutrals (here l=1,2,3).

Reaction	Rate constant (cm^3/s)	Reference
$C_{2l}H^- + ArH^+ \rightarrow C_{2l}H + H + Ar$	3.0×10^{-8}	[15]
$C_{2l}H^- + C_2H_2 \rightarrow C_{2l+2}H^- + H_2$	1.0×10^{-12}	[18]
$C_{2l}H^- + C_mH_n^+ \rightarrow C_{2l}H + C_mH_n$	5.0×10^{-8}	[18]
$C_{2l}H^- + Ar^+ \rightarrow C_{2l}H + Ar$	1.01×10^{-7}	[20]
$C_{2l}H^- + H \rightarrow C_{2l}H_2 + e^-$	1.6×10^{-9}	[50]

The main reactions of our model for collisions of C_2H_2, C_4H_2 and H_2 molecules with plasma species are shown in tables 2, 3 and 4.

Table 2. Main reactions for collisions of electrons with C_2H_2 and H_2 molecules.

Reactions between electrons and hydrocarbons [51, 52]	
$e^- + C_2H_2 \rightarrow C_2H_2^+ + 2e^-$	$e^- + C_2H_2 \rightarrow C_2 + 2H + e^-$
$e^- + C_2H_2 \rightarrow H^+ + C_2H + e^-$	$e^- + C_2H_2 \rightarrow C_2H^+ + H + 2e^-$
$e^- + C_2H_2 \rightarrow C_2H^- + H$	$e^- + C_2H_2 \rightarrow C_2 + H_2 + e^-$
$e^- + C_2H_2 \rightarrow C_2H + H + e^-$	$e^- + C_2H_2 \rightarrow C_2^+ + H_2 + 2e^-$
Reactions between electrons and H_2 [53]	
$e^- + H_2 \rightarrow 2H + e^-$	$e^- + H_2 \rightarrow H^+ + H + 2e^-$
$e^- + H_2 \rightarrow H_2^+ + 2e^-$	

Table 3. Ion-molecular reactions with participation of positive ions accompanied by production and loss of C_2H_2, C_4H_2 and H_2 molecules.

Reaction	Rate constant (cm^3/s)	Reference
Reactions between Ar^+/ArH^+ and neutrals		
$Ar^+ + C_2H_2 \rightarrow C_2H_2^+ + Ar$	4.2×10^{-10}	[20, 54]
$Ar^+ + C_4H_2 \rightarrow C_4H_2^+ + Ar$	4.2×10^{-10}	
$Ar^+ + H_2 \rightarrow ArH^+ + H$	8.7×10^{-10}	[43]
$Ar^+ + H_2 \rightarrow H_2^+ + Ar$	1.8×10^{-11}	[43]
$ArH^+ + C_2H_2 \rightarrow C_2H_2^+ + H + Ar$	4.2×10^{-10}	
$ArH^+ + H_2 \rightarrow H_3^+ + Ar$	6.3×10^{-10}	[43]
Reactions between hydrocarbon ions and molecules		
$C_2H_2^+ + C_2H_2 \rightarrow C_4H_2^+ + H_2$	$0.43\times1.2\times10^{-9}$	[55]
$\rightarrow C_4H_3^+ + H$	$0.49\times1.2\times10^{-9}$	
$\rightarrow C_4H_4^+$	$0.08\times1.2\times10^{-9}$	
$C_2H_2^+ + C_4H_2 \rightarrow C_4H_2^+ + C_2H_2$	$0.9\times1.4\times10^{-9}$	[56]
$\rightarrow C_6H_3^+ + H$	$0.1\times1.4\times10^{-9}$	
$C_2H_2^+ + H_2 \rightarrow C_2H_3^+ + H$	1.0×10^{-11}	[18, 56]
$C_2H_3^+ + C_2H_2 \rightarrow C_4H_3^+ + H_2$	2.4×10^{-10}	[18]
$C_2H_3^+ + H \rightarrow C_2H_2^+ + H_2$	6.8×10^{-11}	[56]
$C_2H_3^+ + C_4H_2 \rightarrow C_4H_3^+ + C_2H_2$	3.0×10^{-10}	[57]
$C_2H_3^+ + C_2H \rightarrow C_2H_2^+ + C_2H_2$	3.3×10^{-10}	[58]
$C_2H_3^+ + C_2H \rightarrow C_4H_2^+ + H_2$	3.3×10^{-10}	[58]
$C_4H_2^+ + C_2H_2 \rightarrow C_6H_4^+$	2.0×10^{-10}	[55, 59]
$C_4H_2^+ + C_4H_2 \rightarrow C_6H_2^+ + C_2H_2$	$0.83\times1.4\times10^{-9}$	[56]
$\rightarrow C_8H_2^+ + H_2$	$0.17\times1.4\times10^{-9}$	
$\rightarrow C_8H_3^+ + H$	$0.01\times1.4\times10^{-9}$	
$C_4H_3^+ + C_4H_2 \rightarrow C_6H_3^+ + C_2H_2$	7.4×10^{-10}	[56]
$C_4H_3^+ + C_2H_2 \rightarrow C_6H_5^+$	2.2×10^{-10}	[56]
$C_6H_4^+ + C_2H_2 \rightarrow C_8H_6^+$	7.0×10^{-11}	[55]

Table 4. Molecule/atom – molecule/atom reactions accounted for in the model. Here T_{gK} is the gas temperature in K, Ar* denotes argon atoms in various excited states including the metastable and 4s and 4p resonance states.

Reaction	Rate constant (cm^3/s)	Reference
Reactions between hydrocarbons		
$C_2H + C_2H_2 \rightarrow C_4H_2 + H$	1.3×10^{-10}	[18]
$C_2H + C_4H_2 \rightarrow C_6H_2 + H$	6.5×10^{-11}	[18]
$C_2H + C_4H_2 \rightarrow C_6H_2^* + H$	6.5×10^{-11}	[18]
Reactions between H/H₂ and hydrocarbons		
$H + C_2H \rightarrow C_2H_2$	$1.66\times10^{-7}/T_{gK}$	[17]
$H + C_2H_2 \rightarrow C_2H_3$	$7.25\times10^{-12} T_{gK}^{-11.67} \times \exp(-1212.7/T_{gK})$	[18]
$H + C_4H_2 \rightarrow C_4H_3$	$2.82\times10^{25} T_{gK}^{-11.67} \times \exp(-6441.0/T_{gK})$	[18]
$H_2 + C_2H \rightarrow C_2H_2 + H$	$1.82\times10^{-11} \times \exp(-1443.0/T_{gK})$	[18]
Reactions with participation of argon atoms in excited states		
$Ar^* + C_2H_2 (C_4H_2) \rightarrow C_2H_2^+ (C_4H_2^+) + Ar + e^-$	0.9×10^{-10}	
$Ar^* + C_2H_2 (C_4H_2) \rightarrow C_2H (C_4H) + Ar + H$	1.75×10^{-10}	
$Ar^* + C_2H_2 (C_4H_2) \rightarrow C_2H_2 (C_4H_2) + Ar + \hbar\omega$	2.65×10^{-10}	
$Ar^* + H_2 \rightarrow ArH^* + H$	1.1×10^{-10}	[54]
$Ar_m + Ar_m \rightarrow Ar + Ar^+ + e^-$	6.2×10^{-10}	[60]
$Ar_m + Ar_m \rightarrow 2Ar$	2.0×10^{-7}	[49]
$Ar_m + Ar_r \rightarrow Ar + Ar^+ + e^-$	2.1×10^{-9}	[49]
$Ar(4p) + Ar(4p) \rightarrow Ar^+ + Ar + e^-$	5.0×10^{-10}	[49]
$Ar_m + Ar \rightarrow 2Ar$	2.1×10^{-15}	[49]
$Ar_r \rightarrow Ar + \hbar\omega$	$10^5\ s^{-1}$	[49]
$Ar(4p) \rightarrow Ar + \hbar\omega$	$3.2\times10^7\ s^{-1}$	[49]
$Ar(4p) \rightarrow Ar_m + \hbar\omega$	$3.0\times10^7\ s^{-1}$	[49]
$Ar(4p) \rightarrow Ar_r + \hbar\omega$	$3.0\times10^7\ s^{-1}$	[49]

For most electron-neutral reactions, we use the reaction cross sections σ instead of the rate coefficients. The cross sections determine the rate coefficients, $K = \int_0^\infty \sigma(\varepsilon) F(\varepsilon) d\varepsilon$. The collision reactions for electrons with argon atoms, ions with C_2H and H radicals are also taken into account in the model (they are described in detail in Supporting Information to [28]). For the reactions of electrons with C_4H_2, the cross sections of ionization, dissociation and electron attachment are taken to be the same as the corresponding cross sections for the reactions of electrons with C_2H_2, since no data concerning the cross sections are available in the literature. The cross sections describing the loss of C_2H in collisions with electrons are taken from [51]. Considering the collisions of argon atoms in excited states Ar* (Ar_m, Ar_r or Ar(4p)) with C_2H_2 and C_4H_2 molecules (table 4), we assume that there are a few pathways of the reactions: $Ar^* + C_2H_2 (C_4H_2) \rightarrow C_2H_2^+ (C_4H_2^+) + Ar + e^-$ with the rate 0.9×10^{-10} cm^3/s, $Ar^* + C_2H_2(C_4H_2) \rightarrow C_2H(C_4H) + Ar + H$ with the rate 1.75×10^{-10} cm^3/s, $Ar^* + C_2H_2 (C_4H_2) \rightarrow C_2H_2^* (C_4H_2^*) + Ar$ (or $C_2H_2(C_4H_2) + Ar + \hbar\omega$) with the rate 2.65×10^{-10} cm^3/s. Note that at present the rates for these reactions are not known. Meantime, the total rate describing the loss of argon metastable atoms in collisions with C_2H_2 ($k_q = 5.6\times10^{-10}$ cm^3/s [61]) was measured. Thus, in this model the total rate for loss of Ar_m in collisions with C_2H_2 is nearly the same as the rate in [61]. More information on the different reactions and rates for various generation and loss processes, as well as elastic and inelastic collisions taken in to account in the power balance (equation (4)), can be found in [15, 28] and in Supporting Information to [28].

3. Results

3.1. Time-dependencies for plasma parameters and their comparison with experimental data

Using the theoretical model presented in section 2, we have analyzed how main plasma parameters (neutral, ion and electron densities, effective electron temperature and dust charge) evolve as dust radius increases with time. These simulations have been performed for conditions similar to our experiments on nanoparticle growth.

Based on our experimental observations, we have made the following assumptions concerning the time-variation of a_d: The duration of a nanoparticle-growth cycle is 108 s. Here we shall separate one growth cycle into two phases: During the first 20 s (phase I), the nanoparticle size is small and the nanoparticles do not modify any plasma properties. In the model, it has been assumed that the dust density equals zero for phase I. For the next 88 s (phase II), the dust radius increases linearly from 10 nm up to 70 nm at a fixed dust density (~ 10^7 cm^{-3}). At the end of a growth cycle, dust particles leave the plasma (because of effect of different forces) and a new growth cycle starts. Note that in our previous works [15, 24] one growth cycle was separated into three phases. The measurable diameter of dust particles was in the range 20-40 nm, 40-50 nm and 50-140 nm for the growth phases I, II and III, respectively. Here, to simplify the 0D model, we divide one growth cycle only in two phases, phase I without particles, phase II with constantly growing particles.

Using the model, we have also calculated the dust radius as a function of time, assuming that the growth of nanoparticles with $a_d > 10$ nm is due to deposition of C_2H radicals and different hydrocarbon ions and compared this evolution with the experiment [24].

In figure 1(*a*), the calculated densities of C_2H_2, C_4H_2, H_2, C_2H and H as a function of time are shown. The time-dependencies are obtained assuming that the dust density in the phase II is 1.5×10^7 cm^{-3} and the phases I and II start at t = 8 s and t = 28 s, respectively. Note that figure 1 shows cycles taken in a middle of a long sequence, so before 8 s it is the end of phase II from another cycle.

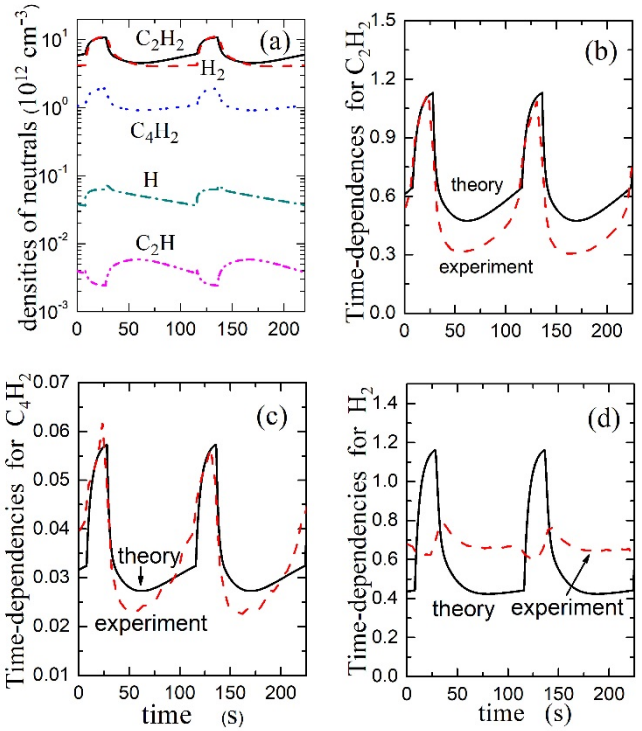

Figure 1. The calculated densities of neutral species (*a*). The mass peaks (experiment) and the normalized calculated densities of neutral species (theory) for C_2H_2 (*b*), C_4H_2 (*c*) and H_2 (*d*).

In figures 1(*b*), 1(*c*) and 1(*d*), the normalized calculated densities of C_2H_2, C_4H_2, H_2 are compared with the intensities of the mass peaks (in a.u.) measured in our experiments [15]. The calculated densities of C_2H_2 and C_4H_2 are normalized on 9.56×10^{12} cm^{-3} to have the calculated maximums of these densities nearly the same as the maximums for the mass peaks in the experiment, while the density of H_2 is normalized on 3.346×10^{13} cm^{-3} (this normalization makes the calculated time-averaged density of H_2 approximately the same as the averaged measured intensity of H_2).

The calculated densities of C_2H_2, C_4H_2 and H_2 are increasing during phase I. For phase II, C_2H_2 and C_4H_2 densities first decrease, reach a minimum and then increase. The time dependency for C_2H_2, H_2 and C_4H_2 is caused, in our opinion, mainly by the time variation for argon atoms in excited states, for electrons, C_2H radicals and for positive ions since the nonradical species are mainly lost in collisions with these species (tables 2-4). The decrease of C_2H_2 and C_4H_2 densities in phase II is due to an enhancement of the losses of these nonradical species in collisions with excited argon atoms, positive ions and radicals. The densities of C_2H_2 and C_4H_2 increase at large times in phase II due to a reduction in n_e, n_m and n_{C2H} (figures 1(*a*) and 2) with growing dust radius.

Since the loss of C_2H_2 molecules is essentially affected by their collisions with excited argon atoms and C_2H radicals [28], their time-dependency is nearly the inverse to those for Ar_m and C_2H (figures 1(*a*), 1(*b*) and 2(*a*)). Therefore, the minimum in n_{C2H2} is nearly at the same time as the maximums for Ar_m and C_2H. During phase I (when the effect of dust particles on plasma parameters is small) which follows after phase II, the density of acetylene is growing because of little losses in different collisions. The C_4H_2 and H_2 production is related to the C_2H_2 density [11], and, as a result, the time-dependencies for the C_4H_2 and H_2 densities (for H_2, excepting the end of phase II) are similar to that for n_{C2H2}.

Note that due to the loss of acetylene molecules in different collisions, the maximum magnitude of C_2H_2 density in the non-stationary plasma with growing dust particles (1.08×10^{13}cm^{-3}) is much smaller than the acetylene density in the chamber in the power-off case (1.38×10^{14}cm^{-3}).

Results of calculations for C_2H_2 and C_4H_2 are similar to the experimental time-dependencies for the mass peaks of C_2H_2 and C_4H_2 (figures 1(*b*) and 1(*c*)), while for H_2 they are partly different (figure 1(*d*)). In particular, in the experiment the intensity of H_2 mass peak in the beginning of phase I is decreasing, while the calculated density increases. Moreover, the difference between maximum and minimum magnitudes of mass peaks is nearly 30%, while the calculated maximum of H_2 density is nearly 3 times larger than the minimum (figure 1(*a*) and figure 1(*d*)). Meantime, the time-dependence for the calculated n_{H2} and the measured mass peak intensity of H_2 behave nearly the same way during most of phase II.

The density of C_2H decreases during phase I, increases in the beginning of phase II, reaches a maximum and then decreases during most of phase II (figure 1(*a*)). The density of atomic hydrogen increases during phase I and the beginning of phase II and then decreases. The densities of neutral species vary mainly due to the collection of electrons, ions and radicals by the dust particles [15, 28]. The reduction of free electrons increases the effective electron temperature during phase II (figure 2(*a*)) when a_d becomes larger.

During phase II, n_e slowly drops down by a factor of 10 because of an enhancement of the electron collection by the dust particles. When the dust particles leave the discharge at the end of a growth cycle, the electron density increases rapidly because of vanishing the electron loss and the energy

loss of electrons on dust particles. Due to a growing temperature T_{eff}, the density of metastable argon atoms becomes larger in the time interval 28 s < t< 65 s (figure 2(*a*)). For 65 s < t< 116 s, n_m drops because of the reduction in n_e. In phase I, the density of metastable argon atoms is dropping because of a lower n_m production as compared with the phase II (T_{eff} is smaller in phase I) as well as due to the enhancement of the n_m loss in collisions with nonradical neutrals (their densities are growing with time). Furthermore, the increase of T_{eff} in phase II also enhances the production of Ar^+ in electron-atom collisions (figure 3). For the same reason the densities of $C_2H_2^+$, $C_4H_2^+$, $C_4H_3^+$, $C_6H_4^+$ and ArH^+ are also increasing at the beginning of phase II. Afterwards, their densities are decreasing because of a reduction of their production at lower electron density and due to the enhancement of their losses in collisions with larger dust particles. The density of $C_2H_3^+$ is found to be smaller (not shown in figure 3) than that of other ions, which agrees well with results of our previous studies [15].

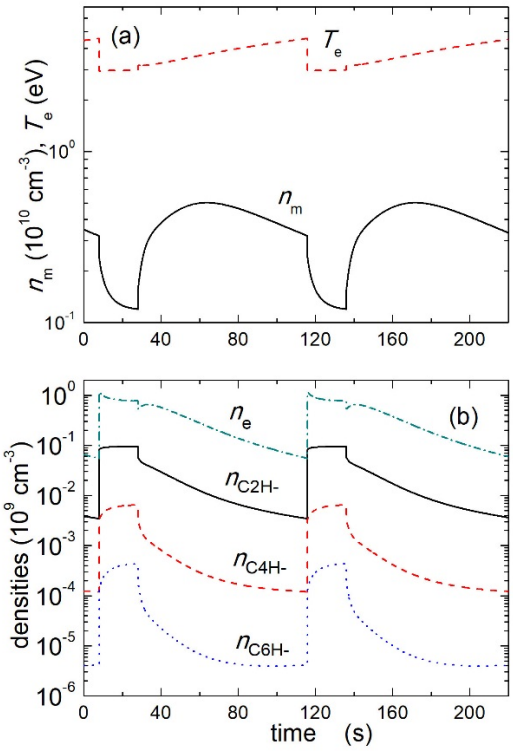

Figure 2. The density of metastable argon atoms and the effective electron temperature (*a*), and the densities of electrons and negative ions (*b*) as function of time.

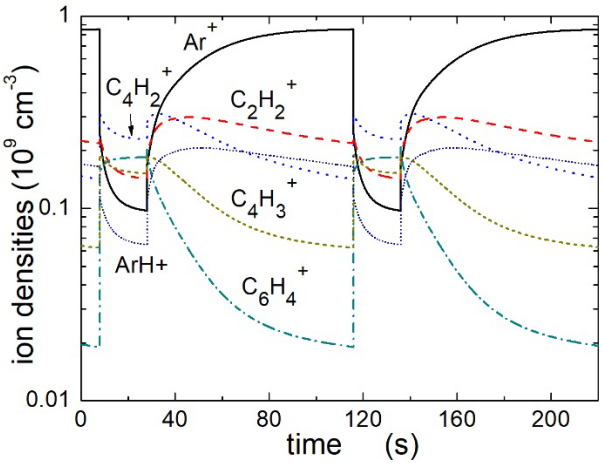

Figure 3. The densities of positive ions as function of time.

The C_2H^- anions are produced in collisions of electrons with acetylene molecules, while they are mainly lost in collisions with positive ions and hydrogen atoms [28]. As a result, the rapid increase of n_e in the beginning of phase I (as n_d is set to 0) is also accompanied by the rapid increase in C_2H^- density (figure 2(*b*)). The density of C_2H^- anions decreases as n_e during phase II and also because of the growing Ar^+ density, which enhances the C_2H^- losses. The time-dependencies for C_4H^- and C_6H^- are similar to the one of C_2H^- because their loss mechanisms are the same, and because the production of C_4H^- and C_6H^- is, respectively, in collisions of C_2H^- and C_4H^- with C_2H_2 (table 1). During phase II, the dust charge increases in time because of the growing surface of the electron collecting dust particles (figure 4(*a*)). The dust charge saturates at the end of phase II because of the extreme electron rarefaction and the high current of positive ions Ar^+ onto the dust.

Using equation (6), we have also calculated the dust radius as a function of time (figure 4(*b*)). The calculations have been carried out for different densities of dust material ρ_d= 1 g/cm^3, 1.5 g/cm^3 and 2 g/cm^3, assuming that the dust radius is 10 nm at the beginning of phase II. The calculated radii are in a good qualitative agreement with the experimental measurements presented in [24]. Naturally, by lowering the dust material density, the calculated dust radius increases (figure 4(*b*)).

We have also obtained the time-dependences for the dust radius assuming that only C_2H radicals take part in the growth of dust particles (in equation (6), $\sum_\alpha K_d^\alpha m_\alpha^+ n_\alpha^+ = 0$), as well as when only hydrocarbon ions affect the growth (in equation (6), $K_d^{C2H} = 0$). The radius evolution for both cases is shown in figure 4(*c*) showing that the growth of dust particles during phase II is mainly related to the deposition of hydrocarbon ions on the surface of dust particles, the C_2H radicals do not affecting much the dust particle growth.

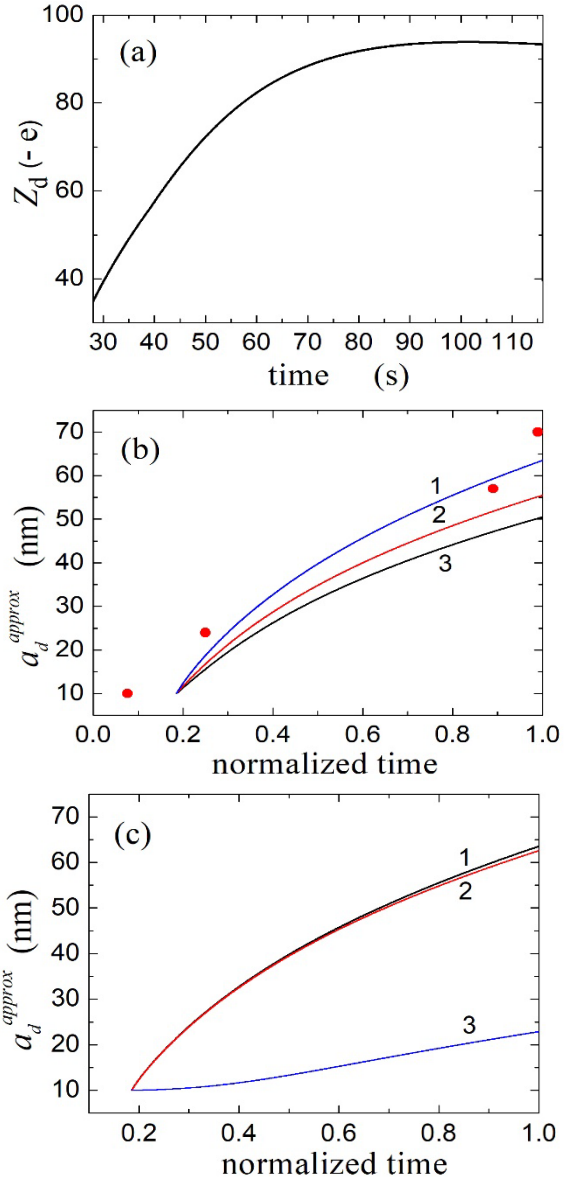

Figure 4. The dust charge as a function of time (*a*). The dust radius obtained from equation (6) for different densities of dust material: $\rho_d = 1.0$ (curve 1), 1.5 (curve 2) and 2.0 (curve 3) g/cm^3 and the measured dust radius (circles) from [24] (*b*). a_d^{approx} calculated assuming that both C_2H radicals and hydrocarbon ions (curve 1), only hydrocarbon ions (curve 2) and only C_2H radicals participate to the growth of dust particles for $\rho_d = 1.0$ g/cm^3 (*c*). The normalized time 0 and 1.0 in figures 4(*b*) and 4(*c*) corresponds to, respectively, $t =$ 8 s and 116 s in figure 1.

3.2. Effects of dust density variation

The dust density during phase II n_d is unknown from our experiments. Therefore, let us analyze how the results of our calculations depend on n_d.

In figure 5, densities of nonradical neutrals and n_H as a function of time are shown for different dust densities: $n_d = 5\times10^6$, 10^7, 1.5×10^7 and 1.8×10^7 cm^{-3}. At small dust density (~ 5×10^6 cm^{-3}) densities of nonradical species are monotonically decreasing with time. For larger n_d ($\geq10^7$ cm^{-3}), densities of C_2H_2 and C_4H_2 decrease at the beginning of phase II, reach a minimum and then increase. The minimums are observed at smaller times when n_d becomes larger (figures 5(*a*) and 5(*c*)). Moreover, densities of C_2H_2, H_2 and C_4H_2 molecules decrease faster with growing n_d at the beginning of phase II (figures 5(*a*), 5(*b*) and 5(*c*)). The n_d dependency for C_2H_2, H_2 and C_4H_2 is caused mainly by the density variation for argon atoms in excited states, for electrons, C_2H radicals and for positive ions. The density of atomic hydrogen increases at the beginning of phase II but then decreases during the rest of the phase (figure 5(*d*)). This increase is mainly due to enhancement of the H production in collisions of excited argon atoms, Ar^+ ions and C_2H radicals (their densities increase at the beginning of phase II (figures 3, 6(*a*) and 6(*b*))) with nonradical neutrals, while the decrease is also caused by production changes through the lowering of the nonradical densities at the first half of phase II and through the lowering of Ar_m and C_2H densities at the second half of phase II. The H density becomes larger during phase I mainly because of rising densities of nonradical species, from which H mainly originates. Its decrease with increasing n_d during phase II is mainly due to the decrease of the densities of electrons (figure 6(*c*)) and H_2 molecules (figure 5(*b*)) and due to the decrease of n_m and n_{C2H} in the second part of phase II (figures 6(*a*) and 6(*b*)). Note that the production of atomic hydrogen in Ar/C_2H_2 plasmas is mainly due to collisions of Ar* with C_2H_2, C_4H_2 and H_2, of Ar^+ with H_2 and of C_2H with C_2H_2 and C_4H_2, as well as due to electron-impact dissociation and ionization of H_2 molecules (Supporting information to [28]).

With higher n_d, the density of Ar_m increases faster in the beginning of phase II (figure 6(*a*)) due to the likewise accelerated increase of T_{eff} (figure 6(*d*)). The metastable density then goes to a maximum, which is reached the earlier the higher is the dust density because of the enhancement of their losses in collisions with nonradical neutrals. The densities of C_2H_2 and C_4H_2 increase at large times in phase II (figures 5(*a*) and 5(*c*)) due to a reduction in n_e, n_m and n_{C2H} (figure 6) with growing dust density. As it was already noted in previous subsection, the time-dependency for C_2H_2 is nearly the inverse to those for Ar_m and C_2H (figures 5(*a*), 6(*a*) and 6(*b*)).

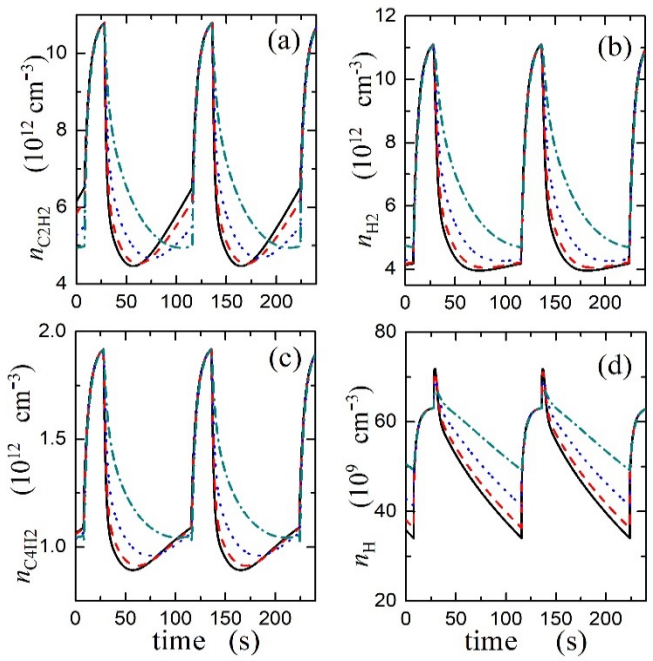

Figure 5. The densities of C_2H_2 (*a*), H_2 (*b*), C_4H_2 (*c*) and H (*d*) for different dust densities in the dust-growth phase: n_d = 5×10^6 (dash-dotted curves), 10^7(dotted curves) 1.5×10^7 (dashed curves) and 1.8×10^7 (solid curves) cm^{-3}.

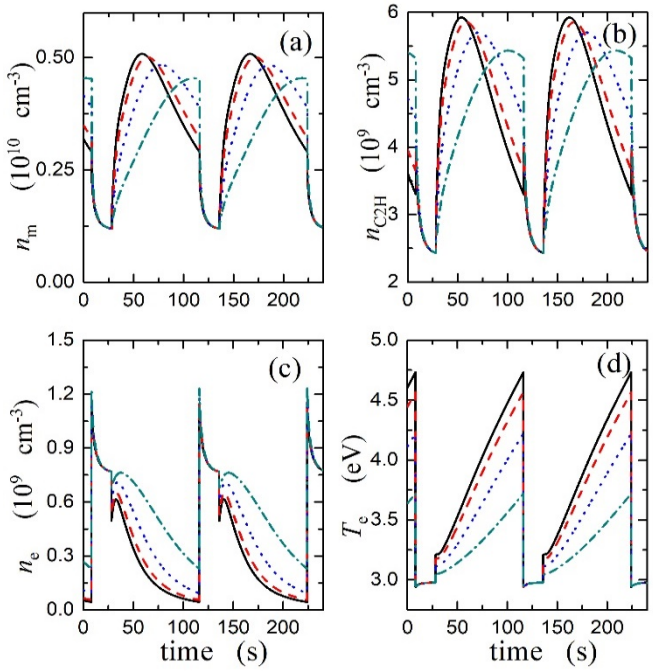

Figure 6. The density of metastable argon atoms (*a*), C2H density (*b*), electron density (*c*) and effective electron temperature (*d*), for different dust densities in the dust-growth phase: n_d = 5×10^6 (dash-dotted curves), 10^7(dotted curves) 1.5×10^7 (dashed curves) and 1.8×10^7 (solid curves) cm^{-3}.

Therefore, the minimum in n_{C2H2} is reached earlier with high n_d and it is accompanied by the early maximum of the C_2H (figure 6(*b*)) and $C_2H_2^+$ (figure 7(*a*)) densities and by the more rapid growth of Ar^+ density (figure 7(*b*)) during phase II.

The faster increase of densities of the latter species in the beginning of phase II is due to, at least in part, an increase of T_{eff} that enhances their production in collisions of electrons with neutrals.

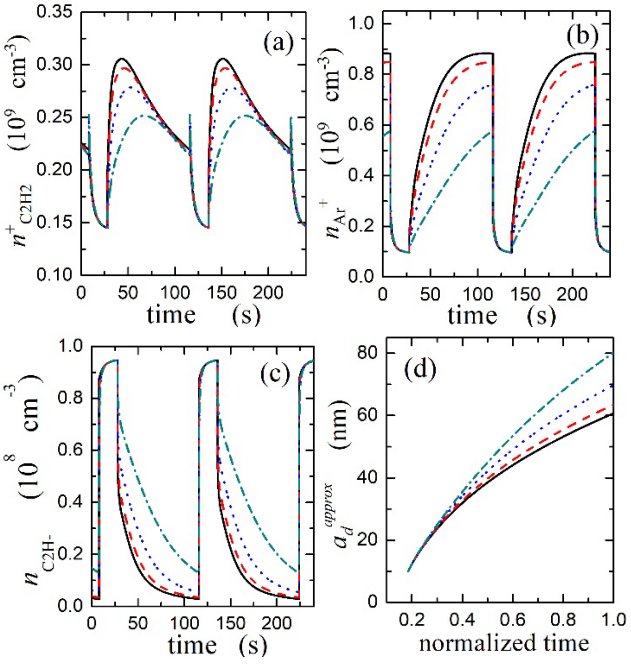

Figure 7. Densities of $C_2H_2^+$ (*a*), Ar^+ (*b*) and C_2H^- ions (*c*) and the calculated dust radius (*d*) for different dust densities in the dust-growth phase: n_d = 5×10^6 (dash-dotted curves), 10^7(dotted curves), 1.5×10^7 (dashed curves) and 1.8×10^7 (solid curves) cm^{-3}. The other conditions are the same as in figure 6. In figure 7 (*d*), $\rho_d = 1.0$ g/cm^3 and the normalization of time is the same as for figure 4(*b*).

The density of negative ions in phase II decreases when n_d increases (figure 7(*c*)), mainly due to the enhancement of the anion losses in collisions with Ar^+ and $C_2H_2^+$ ions, whose densities grow with n_d (figures 7(*a*) and 7(*b*)).

Note that the calculated dust radius a_d^{approx} decreases when n_d increases (figure 7(*d*)). This can be explained by a smaller amount of available hydrocarbon positive ions and C_2H radicals per dust particle for the same input of acetylene.

4. Discussion and summary

In this paper, we investigated through 0D simulations the physics and chemistry of an Ar/C_2H_2 plasma containing growing dust particles. One of the main goals of this work was to obtain the time-dependencies of different plasma parameters (ion, electron and neutral particle densities, effective electron temperature and dust charge) for the conditions of our experiments [24]. Especially, comparisons

between the calculated time-dependencies of C_2H_2, H_2 and C_4H_2 with the time-dependencies of corresponding mass-peaks measured experimentally. We also studied how our calculations depend on the density of dust particles, which is unknown from our experiments. The evolution of the dust radius is also calculated during dust particle growth as a function of calculated reactant flux towards their surface.

The calculated time-dependencies of C_2H_2 and C_4H_2 are in a good agreement with the experimental data. During phase I (when the effect of dust particles on plasma parameters is small), the density of acetylene is growing because of little losses in different collisions. On the contrary, in the beginning of the accretion phase, the acetylene density drops rapidly because of a strong enhancement of the losses with excited argon atoms, positive ions and radicals. These latter species are highly produced due to a T_{eff} increase related to an enhanced collection of electrons and ions by dust particles. Surprisingly, at larger times in the accretion stage, the acetylene density increases again mainly because of smaller losses. While T_{eff} increases, its effect is dominated by the strong decrease of n_e (and thus species produced by electron collision) due to electron collection by dust particles.

The minimum in the densities of C_2H_2 and C_4H_2 during phase II is non-intuitive. Additionally, we show that it appears earlier when increasing the dust density. This is mainly due to the impact of the dust density on Ar_m, positive ions and C_2H radicals. With the increase of the dust density, the effective electron temperature becomes larger and grows faster, while the electron density in the accretion stage becomes smaller. As a result, the densities of non-radical neutrals drop faster in the beginning of the accretion stage. At the end of phase II, the densities of C_2H_2 and C_4H_2 increase with increasing the dust density because of smaller losses of these molecules in collisions with electrons, excited argon atoms and C_2H radicals (their densities drop with increasing n_d). Note that the non-linear behavior of most densities during the linear growth of particles can be explained in our calculations without variation in the dust density.

The growth of the dust radius during the accretion stage is calculated for different dust material densities and number densities assuming that only C_2H radicals and positive hydrocarbon ions take part in the growth. The calculated time-dependency appears to be in reasonable agreement with experimental data throughout the dust number density and mass density range used in our calculations (see figures 4 and 7d). This suggests that the positive ion deposition on dust particles is effectively the dominant growth mechanism.

Meantime, there is a discrepancy between our calculations and the experimental data for hydrogen molecules, especially in phase I when dust particles do not affect much the plasma properties. In our opinion, the discrepancy is mainly caused by some simplifications used in the 0D model. In particular, the model here assumes that phase I is immediately followed by the accretion phase without considering any intermediate coagulation stage.

In [62], it was shown that plasma parameters in the coagulation phase may change strongly in argon/silane plasma if the dust density at the end of the coagulation phase is large ($>10^8$ cm^{-3}). Meantime, here we consider much smaller dust densities in the accretion stage ($\sim10^7$ cm^{-3}), and, therefore, we expect that the effect of the coagulation of nanoparticles in our Ar/C_2H_2 plasma is not as strong as in [62].

The model does not account for plasma inhomogeneity effects neither, which may be very important, in particular, at the end of the accretion stage when the formation of a void may take place [2, 63]. Moreover, the model does not account for effects of dust particles on the shape of electron energy distribution function. Meantime, it was shown that for sufficiently high dust density and/or size, in a low-pressure argon glow discharge, the Druyvesteyn-like electron distribution in dust-free plasmas can become nearly Maxwellian [64, 65]. Hence, the shape of the electron energy distribution function in the dust-free phase may be different from the one in the accretion phase when the plasma contains dust particles with large sizes and densities.

Note that here the approximate time-dependency for the dust radius a_d^{approx} (figures 4(*b*) and 4 (*c*)) has not been obtained self-consistently with other plasma parameters. Getting this time-dependency, the densities of plasma species, effective electron temperature and dust charge as a function of time have been obtained from equations (1)-(5), assuming that the dust radius grows linearly with time in the accretion stage. Moreover, equation (6) does not account for any loss of the dust material, in particular due to sputtering from ion bombardment [66]. Here we assume that the loss of dust material due to sputtering is not important because ions bombarding dust particles have rather small energies (a few eV). For example, the energy threshold for argon ions sputtering hydrocarbons is in the order of a few tens of eV. Regarding the growth of dust particles, we also do not account for chemical etching.

Therefore, the model here is applicable only for a qualitative analysis of argon/acetylene plasmas containing growing dust particles and it should be improved by inclusion of effects related to spatial plasma inhomogeneity, changes of the EEDF shape, inclusion of the processes describing the loss of dust material, as well as by inclusion of the coagulation stage.

Meantime, our model has some advantages compared to previous models of argon/acetylene dust-forming plasmas currently available in the literature. Besides accounting for the effect of dust particles on the plasma properties, it allows to obtain the plasma parameters as a function of time. Moreover, the model is rather simple, accounts for main species measured in our experiments and gives a good agreement with experimental data. The obtained results are relevant for many

applications involving reactive plasmas [67], especially gas discharges used for the synthesis of various nanomaterials.

Acknowledgements

The authors acknowledge the financial support of the Deutsche Forschungsgemeinschaft in the frame of the project B13 of the SFB/Transregio 24. J B and E K would like to acknowledge the support from French Research Agency via ANR project PLASMABOND.

[1] Bouchoule A (ed) 1999 *Dusty Plasmas: Physics, Chemistry, and Technological Impacts in Plasma Processing* (New York: Wiley)
[2] Vladimirov S V and Ostrikov K 2004 *Phys. Rep.* 393 175
[3] Ostrikov K, Cvelbar U and Murphy B 2011 *J. Phys. D: Appl. Phys.* **44** 174001
[4] Mikikian M *et al* 2017 *Plasma Phys. Control. Fusion* 59 014034
[5] Hong S, Berndt J and Winter J 2003 *Plasma Sources Sci. Technol.* **12** 46
[6] Deschenaux C, Affolter A, Magni D, Hollenstein C and Fayet P 1999 *J. Phys. D: Appl. Phys.* **32** 1876
[7] Benedikt J, Consoli A, Schulze M and von Keudell A 2007 *J. Phys. Chem. A* **111** 10453
[8] Thejaswini H C, Peglow S, Martens U, Sushkov V and Hippler R 2014 *Contrib. Plasma Phys.* **54** 683
[9] Do H T, Thieme G, Fröhlich M, Kersten H and Hippler R 2005 *Contrib. Plasma Phys.* **45** 378
[10] Winter J, Berndt J, Hong S H, Kovačević E, Stefanović I and Stepanović O 2009 *Plasma Sources Sci. Technol.* **18** 034010
[11] Herrendorf A P, Sushkov V and Hippler R 2017 *J. Appl. Phys.* **121** 123303
[12] Berndt J, Kovačević E, Stefanović I and Boufendi L 2009 *J. Appl. Phys.* **106** 063309
[13] Stefanović I, Sadeghi N, Winter J and Sikimić B 2017 *Plasma Sources Sci. Technol.* **26** 065014
[14] Wegner T, Hinz A M, Faupel F, Strunskus T, Kersten H and Meichsner J 2016 *Appl. Phys. Lett.* **108** 063108
[15] Denysenko I B, von Wahl E, Labidi S, Mikikian M, Kersten H, Gibert T, Kovačević E and Azarenkov N A 2019 *Plasma Phys. Control. Fusion* **61** 014014
[16] Stoykov S, Eggs C and Kortshagen U 2001 *J. Phys. D: Appl. Phys.* **34** 2160
[17] Bleecker K De, Bogaerts A and Goedheer W 2006 *Phys. Rev. E* **73** 026406
[18] Mao M, Benedikt J, Consoli A and Bogaerts A 2008 *J. Phys. D: Appl. Phys.* **41** 225201
[19] Ariskin D A, Schweigert I V, Alexandrov A L, Bogaerts A and Peeters F M 2009 *J. Appl. Phys.* **105** 063305
[20] Schweigert I V, Alexandrov A L and Ariskin D A 2014 *Plasma Chem. Plasma Process.* **34** 671
[21] Akhoundi A and Foroutan G 2017 *Phys. Plasmas* **24** 053516
[22] Ostrikov K, Yoon H-J, Rider A E and Vladimirov S V 2007 *Plasma Process. Polym.* **4** 27
[23] Stefanović I, Sadeghi N and Winter J 2010 *J. Phys. D: Appl. Phys.* **43** 152003
[24] Hinz A M, von Wahl E, Faupel F, Strunskus T and Kersten H 2015 *J. Phys. D: Appl. Phys.* **48** 055203
[25] Berndt J, Kovačević E, Stefanović I, Stepanović O, Hong S H, Boufendi L and Winter J 2009 *Contrib. Plasma Phys.* **49** 107
[26] Denysenko I, Berndt J, Kovacevic E, Stefanovic I, Selenin V and Winter J 2006 *Phys. of Plasmas* **13** 073507
[27] Jiménez-Redondo M, Tanarro I, Peláez R J, Díaz-Pérez L and Herrero V J 2019 *J. Phys. Chem. A* **123** 8135
[28] Denysenko I B, Wahl E von, Labidi S, Mikikian M, Kersten H and Gibert T 2019 *Plasma Processes and Polymers* **16** 1800209
[29] Gudmundsson J T 2001 *Plasma Sources Sci. Technol.* **10** 76
[30] Godyak V A, Piejak R B and Alexandrovich B M 1992 *Plasma Sources Sci. Technol*. **1** 36
[31] Thorsteinsson E G and Gudmundsson J T 2009 *Plasma Sources Sci. Technol.* **18** 045001
[32] Lieberman M A and Gottscho R A 1994 *Physics of Thin Films* vol 18 edited by M Francombe and J Vossen (New York: Academic) pp 1–119
[33] Denysenko I, Yu M Y, Ostrikov K and Smolyakov A 2004 *Phys. Rev. E* **70** 046403
[34] Khrapak S A, Ratynskaia S V, Zobnin A V, Usachev A D, Yaroshenko V V, Thoma M H, Kretschmer M, Hofner H, Morfill G E, Petro O F and Fortov V E 2005 *Phys. Rev. E* **72** 016406
[35] Byrne G D and Thompson S 2013 *VODE_F90 Support Page*, http: //www.radford.edu/~thompson/vodef90web
[36] von Keudell A, Hopf C, Schwarz-Selinger T and Jacob W 1999 *Nucl. Fusion* **39** 1451
[37] Ferrari C, Libassi A, Tanner B K, Stolojan V, Yuan J, Brown L M, Rodil S E, Kleinsorge B and Robertson J 2000 *Phys. Rev. B* **62** 11089
[38] Tadsen B, Greiner F, Groth S and Piel A 2015 *Phys. Plasmas* **22** 113701
[39] Denysenko I B, Xu S, Long J D, Rutkevych P P, Azarenkov N A and Ostrikov K 2004 *J. Appl. Phys.* **95** 2713
[40] Booth J P and Sadeghi N 1991 *J. Appl. Phys.* **70** 611
[41] Marlow W C and Bershader D 1964 *Phys. Rev*. **133** A629
[42] Sode M, Schwarz-Selinger T, Jacob W and Kersten H 2014 *J. Appl. Phys.* **116** 013302
[43] Sode M, Jacob W, Schwarz-Selinger T and Kersten H 2015 *J. Appl. Phys.* **117** 083303
[44] Sikimić B, Stefanović I, Denysenko I B, Winter J and Sadeghi N 2014 *Plasma Sources Sci. Technol.* **23** 025010
[45] Cvelbar U, Mozetič M, Poberaj I, Babič D and Ricard A 2005 *Thin Solid Films* **475** 12
[46] Mcdaniel E W and Mason E A 1973 The mobility and diffusion of ions in gases (New York: John Wiley & Sons)
[47] Hurlbatt A, Gibson A R, Schröter S, Bredin J, Foote A P S, Grondein P, O'Connell D and Gans T 2017 *Plasma Process. Polym*. **14** 1600138
[48] Monahan D D and Turner M M 2008 *Plasma Sources Sci. Technol.* **17** 045003
[49] Hjartarson A T, Thorsteinsson E G and Gudmundsson J T 2010 *Plasma Sources Sci. Technol.* **19** 065008
[50] Barckholtz C, Snow T P and Bierbaum V M 2001 *Astrophys. J.* **547** L171
[51] Janev R K and Reiter D 2004 *Phys. Plasmas*. **11** 780
[52] Rutrowsky J, Drost H and Spangenber H J 1980 *Ann. Phys*. **492** 259
[53] Yoon J S, Song M Y, Han J M, Hwang S H, Chang W S, Lee B J and Itikawa Y 2008 *J. Phys. Chem. Ref. Data* **37** 913
[54] Gordillo-Vazquez F J and Albella J M 2003 *J. Appl. Phys.* **94** 6085
[55] Knight J S, Freeman C G, McEwan M J, Anicich V G and Huntress Jr. W T 1987 *J. Phys. Chem.* **91** 3898

[56] Anicich V and McEwan M 1997 *Planet. Space Sci*. **45** 897
[57] Herbst E and Leung C 1989 *Ap. J. Supl. Ser*. **69** 271
[58] The UMIST Database for Astrochemistry, http://www.udfa.net/
[59] Miasek P G and Beauchamp J L 1979 *In. J. Mass Spectrom. Ion Phys*. **15** 49
[60] Denysenko I, Stefanović I, Sikimić B, Winter J, Azarenkov N A and Sadeghi N 2011 *J. Phys. D: Appl. Phys*. **44** 205
[61] Velazco J E, Kolts J H and Setser DW 1978 *J. Chem. Phys.* **69** 4358
[62] Kortshagen U and Bhandarkar U 1999 *Phys. Rev. E* **60** 887
[63] Mikikian M, Boufendi L, Bouchoule A, Thomas H M, Morfill G E, Nefedov A P, Fortov V E and the PKE-Nefedov Team 2003 *New J. Phys*. **5** 19
[64] Denysenko I B, Kersten H and Azarenkov N A 2015 *Phys. Rev. E* **92** 033102
[65] Denysenko I, Yu M Y , Ostrikov K, Azarenkov N A and Stenflo L 2004 *Phys. Plasmas* **11** 4959
[66] Mantzaris N V, Gogolides E, Boudouvis A G, Rhallabi A and Turban G 1996 *J. Appl. Phys.* **79** 3718
[67] Bazaka K, Levchenko I, Lim J W M, Baranov O, Corbella C, Xu S and Keidar M 2019 *J. Phys. D: Appl. Phys.* **52** 183001